Non-line-of-sight Imaging with Radio Signals

Ying He*, Dongheng Zhang*, Yang Hu†, and Yan Chen†
* School of Information and Communication Engineering, University of Electronic Science and Technology of China
E-mail: heying@std.uestc.edu.cn
† School of Cyberspace Security, University of Science and Technology of China
E-mail: eecyan@ustc.edu.cn

***Abstract*—Non-line-of-sight (NLOS) imaging reconstructs the shape and albedo of objects outside the field of view of an imaging system. Based on this technique, a wide range of applications such as autonomous vehicle navigation, robotic and machine vision, as well as medical imaging will possess unprecedented capabilities. Recent NLOS imaging approaches employ ultra-fast pulsed laser and time-resolved photon detector to collect light transients, which are however time-consuming due to the point-by-point grid scan on the wall. Moreover, the maximum imaging distance is only a few meters because of the limitation of the photon counter. In this paper, we introduce Radio Frequency (RF) NLOS imaging to reconstruct hidden objects with radio signals. By analyzing the image formation model, we transform the reconstruction problem into an optimization problem that can be solved with additional constraints. The simulation results validate that we can reconstruct letter-shaped objects using a 12×12 multiple-input multiple-output (MIMO) array and a stepped frequency signal with a bandwidth of 4GHz. , Compared with the optical NLOS imaging, the proposed method can capture the hidden 3D geometry at longer ranges with shorter acquisition times.**

I. Introduction

Most of the information our brain receives comes from our eyes, which inspires us to transform all kinds of signals such as optical, radio, and acoustic signals into images. By processing the optical images, we can obtain most data of our life, but the non-line-of-sight (NLOS) scene cannot be captured because of the line-of-sight (LOS) limitation of the optical signals. A wide range of applications, including autonomous vehicle navigation, robotic and machine vision, as well as medical imaging would process unprecedented capabilities if the NLOS imaging technique has been implemented.

Recent approaches solve the NLOS imaging challenge by employing the optical imaging system with a pulsed laser and a sensitive time-resolved photon detector to generate and detect photon, respectively. There are mainly two shortcomings of these NLOS imaging approaches: (a) a 2D scanning galvonometer raster is required to scan the visible wall point-by-point, which is very time-consuming; (b) the temporal resolution and maximum stored number of the Time-Correlated Single Photon Counting (TCSPC) module are limited, due to which the maximum detection range is limited (typically smaller than 3 meter) [1]. To overcome the shortcomings, in this paper, we propose to recover the three-dimensional (3D) shapes and localization of hidden objects with radio signals. Compared with optical NLOS imaging approaches, the radio NLOS imaging approach utilizes a MIMO array that enables all receiver antennas to collect data simultaneously, which is orders of magnitude less time-consuming. Furthermore, our system has no limitation on the view distance.

The capability of radio imaging has been demonstrated using different electromagnetic spectrum. The first category is the high-frequency imaging radar with Terahertz spectrum[2], [3], [4], [5]. These systems are intrinsically different from ours since they operate at much higher frequencies where the wavelength is comparable to the roughness of the surface of the object to be reconstructed, making the object becomes a scatterer as opposed to a reflector. The advantage of these systems is the high-resolution imaging quality. However, the high cost of the device makes it less likely to be widely deployed. The second category uses centimeter/milimeter-waves with carrier frequency around a few GHz to tens of GHz. The wide bandwidth and MIMO technique have great potential in providing high-resolution imaging[6], [7]. Consider the home sensing scenarios, our system is motivated by recent advances in wireless research, which has shown that with larger than 1 GHz bandwidth Frequency Modulated Continuous Wave (FMCW) signals, a system can capture the skeleton of a human target using special-purpose hardware [8].

Our system is also aspirated by the optical NLOS imaging techniques, which utilize laser pulse for imaging hidden scenes. The hidden object reflects photons toward the visible scene, which then redirects photons toward the detector. The visible scene can be treated as a virtual array to model NLOS imaging as conventional LOS imaging. Most optical NLOS imaging systems employ time-resolved sensors (e.g., ultra-fast photodiodes [9], streak cameras[10], and single-photon avalanche photon detectors (SPADs)[1]). These sensors record not only the number of incident photons (intensity) but also their arrival times. Then, the image formation models to represent the relationship between time-related measurements and the hidden object are discussed, based on which the inverse problems for transient image reconstruction and geometry recover can be merged into a non-linear optimization problem that can be solved efficiently[11], [12].

In this paper, we present an algorithm that enables computational imaging of objects by leveraging radio multipath propagation. The key motivation of our work is that if the reflection property of the reflector is specular for radio signals, radio NLOS imaging reveals hidden objects more easily since the measurements appear to be captured directly from a virtual mirrored volume located behind the reflector as if the reflector were transparent, as illustrated in Fig.1. In such a case, the

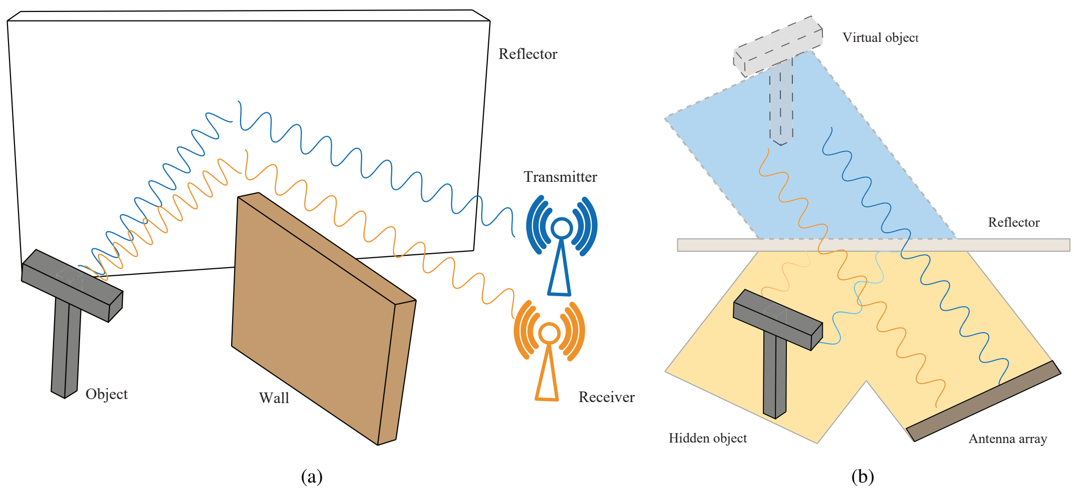

Fig. 1. The illustration of the radio NLOS imaging system: (a) the radio signals are emitted from the transmitter, reflected by the reflector to a hidden object, and then recorded by the receiver; (b) when the reflection property of the reflector is specular, the measurements appear to be captured from a mirrored volume located behind the reflector, as if the wall were transparent.

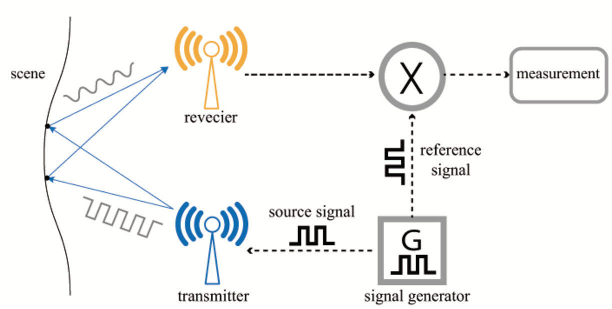

Fig. 2. An illustration of the system model. The temporally modulated source signal is emitted by the transmitter. After reflecting by the scene, the signal is measured by the receiver. The received signal is demodulated by the reference signal to generate the measurement for scene reconstruction.

NLOS imaging is equivalent to the LOS imaging where the signal can reach the object directly. For the radio LOS imaging system, the main challenge is the coupling of the reflections from multiple points of the object. We address this challenge by leveraging a 2D MIMO antenna array and a wide band stepped-frequency signal. There are mainly two components in our system. The first one is the image formation model that illustrates the relationship between measurements and the hidden object. The second one is the reconstruction model that reconstructs the hidden object from the measurements through solving an optimization problem. By including additional regularization term, we solve the optimization problem efficiently to obtain robust reconstruction results.

II. Image formation Model

As illustrated in Fig.1(b), radio NLOS imaging is equivalent to image the virtual mirrored object in the LOS setting. Thus, in the rest of this paper, we focus on how to recover the virtual object. As shown in Fig.2, our system consists of transmitters who provide the temporally modulated radio signal, and receivers who receive the incident signal. The transmitted signal will be affected by the scene before arriving at the receiver. Thus, the characteristics of the scene such as its shape and size will be embedded in the received signal. The image formation model is built to illustrate the relationship between measurements and the object.

A. Matrix multiplication representation of image formation model

Considering a single-path scenario shown in Fig.3(a), the signal emitted from the transmitter at point p_t is reflected once at point p, and then received by the receiver. The distance between point p and the transmitter is d_t, and the distance between point p and the receiver is d_r. Let the source be modulated with a periodic function $s(t)$, then the received signal at point p_r is given as follows

$$r_p(p_t, p_r, t) = s\left(t - \frac{d(p, p_t, p_r)}{c}\right) v(p)\beta(p, p_r, p_t), \tag{1}$$

where $d(p, p_t, p_r) = d_r + d_t$ is the propagation distance, c is the speed of the signal, $v(p)$ is the reflection coefficient at point p, and $\beta(p, p_r, p_t)$ represents the channel characteristics including the reflection, scatter and falloff.

When there are multiple reflection points in the scene, as shown in Fig.3(b), the overall received signal $r(p_t, p_r, t)$ is the integral of contributions from the set of all reflection points as follows

$$\begin{aligned} r(p_t, p_r, t) &= \int r_p(p_t, p_r, t)dp \\ &= \int_p s\left(t - \frac{d(p, p_t, p_r)}{c}\right) v(p)\beta(p, p_r, p_t)dp. \end{aligned} \tag{2}$$

It expresses the temporal signal profiles received at a pixel in terms of the emitted signal $s(t)$ and the scene properties (reflection coefficients, transport coefficients, and path lengths). If $s(t) = e^{j\omega t}$, the received signal is:

$$r(p_t, p_r, t) = s(t) \int_p e^{-j2\pi f \frac{d(p,p_t,p_r)}{c}} v(p)\beta(p, p_r, p_t)dp. \quad (3)$$

The scene can be considered as a system that transforms the signal emitted by the source into the signal received at the destination. To obtain a compact expression of this transformation by matrix multiplication, we combine the reflection coefficient and source signal as a signal emitted to different points as $s(p) = s(t)v(p)$. Then, (3) can be re-written in a matrix form as follows

$$\boldsymbol{R} = \boldsymbol{H}\boldsymbol{S}, \quad (4)$$

where $\boldsymbol{R}$ is the array of the signal received at several sensor pixels and $\boldsymbol{S}$ is the array of the signal emitted by the source to different points. The element of $\boldsymbol{S}$ is $s(p)$. This equation is called the transport equation and $\boldsymbol{H}$ is called the transport matrix of the scene. Compared to conventional transport matrix, the difference of the transport matrix lies in the frequency factor: $e^{-j2\pi f \frac{d(p,p_t,p_r)}{c}}$, i.e., the transport matrix is a function of the modulation frequency f.

As shown in Fig.2, the measurement is generated by multiplying the received signal with the reference signal. We choose the conjunction of the emitted source as the reference signal which is denoted as $s_{ref}(t) = s(t)^*$. After demodulation, we obtain the image formation model, which is a function of modulation frequency and the locations of transmitter/receiver as follows

$$\tau(p_t, p_r, f) = \int_p e^{-j2\pi f \frac{d(p,p_t,p_r)}{c}} v(p)\beta(p, p_r, p_t)d_p. \quad (5)$$

The image formation model can be represented as a matrix form

$$\boldsymbol{\tau} = \boldsymbol{H}\boldsymbol{v}, \quad (6)$$

where $\boldsymbol{H} \in \mathbb{C}^{N\times M}$ is the transport matrix with $\boldsymbol{H}_{nm} = exp(-j2\pi f_i \frac{d(p,p_t,p_r)}{c})\beta(p, p_r, p_t)$.

B. Transport matrix representation

The transport matrix is determined by channel characteristics that contain two parts: 1) distance falloff and time delay caused by signal propagation, which changes both amplitude and phase of the signal; 2) reflection and scattering caused by the interaction of the signal and the scene, which changes only the amplitude of the signal. The effects of channel characteristics are illustrated in Fig.4 and discussed in the following.

1) Reflection and scattering: Reflection and scattering can be modeled by the bidirectional reflectance distribution function (BRDF) which depends on the normalized vector $\boldsymbol{\omega_t}$ pointing from a point p to the transmitter and the normalized direction $\boldsymbol{\omega_r}$ pointing to the receiver. For different size objects with different surface geometries, the observed BRDF varies as illustrated in Fig.5. Specular scattering dominates from surfaces that are on the order of the wavelength in size and flat relative to the wavelength. In this case, BRDF can be modeled as a delta function as given by Snell's law:

$$f_{specular}(\boldsymbol{\omega_t}, \boldsymbol{\omega_r}) = \delta(\boldsymbol{\omega_t} + \boldsymbol{\omega_r} - 2\langle \boldsymbol{n}, \boldsymbol{\omega_t}\rangle \boldsymbol{n}), \quad (7)$$

where $\boldsymbol{n}$ is the surface normal.

A retroreflective effect can be observed from objects with sharp angular geometries and corners, which are larger than the wavelength. The BRDF can also be modeled as a delta

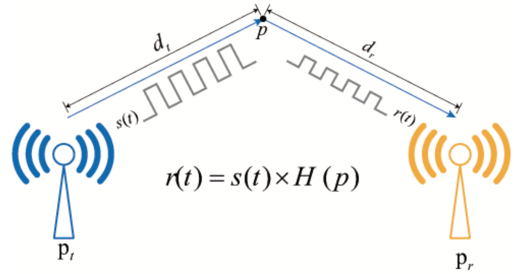

(a) Single path

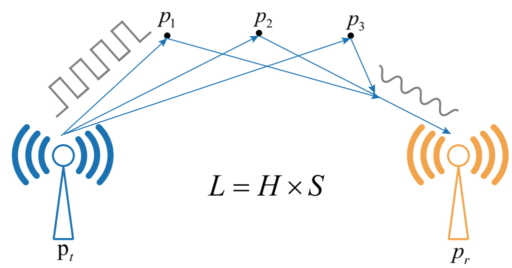

(b) Multipath

Fig. 3. An illustration of the radio transport: (a) rays are emitted from the source and reflected by a point scene, where the scene transforms the emitted signal into the received signal; (b) radio transport along paths between all the emitted and received rays can be compactly represented as a matrix multiplication.

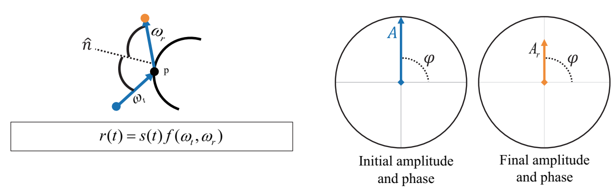

(a) Reflection and scattering

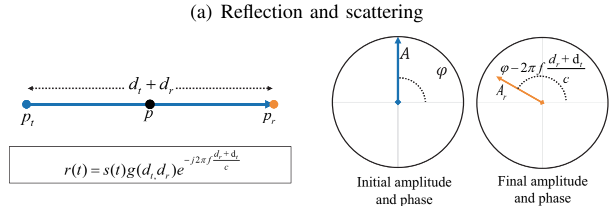

(b) Distance falloff and time delay

Fig. 4. An illustration of channel characteristics effects: (a) the effect of reflection and scattering can be modeled by reflectance distribution function (BRDF) which only changes the amplitude of the signal; (b) the time delay leads to a phase change, and distance falloff cause changes of amplitude.

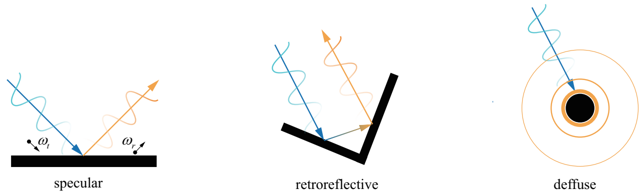

Fig. 5. An illustration of BRDFs. Surfaces that are flat on a scale larger than the wavelength exhibit specular scattering (left). Corner geometries on the scale of the wavelength exhibit retroreflective scattering (center). For surfaces smaller than the wavelength, diffraction around the object causes a diffuse scattering event (right).

function :

$$f_{retroreflective}(\boldsymbol{\omega_t}, \boldsymbol{\omega_r}) = \delta(\boldsymbol{\omega_t} - \boldsymbol{\omega_r}). \tag{8}$$

For surfaces smaller than the wavelength, diffraction around the object causes a diffuse scattering event. In this scenario, the BRDF is Lambertian because the signal is reflected to nearly all directions.

2) Distance falloff and time delay: The distance falloff is the effect that the radio energy attenuates as it propagates through space. It depends on the propagation distance of the signal from the transmitter to the scatter then back to the receiver. For diffuse reflections, the signal falloff is $g(d_t, d_r) = 1/d_t^2 d_r^2$, where d_t and d_r and distances from the reflection point to the transmitter and receiver, respectively. As specular and corner reflections redirect the wavefront rather than causing an additional diffuse scattering event, the distance falloff is proportional to the total propagation distance. The signal falloff is therefore $g(d_t, d_r) = 1/(d_t + d_r)^2$. The time delay causes phase changes of the signal which depends on the propagation distance, transmission speed, and signal frequency: $e^{-j2\pi f \frac{d_t + d_r}{c}}$.

According to the above discussion, the element of the transport matrix can be written as:

$$H_{ij} = e^{-j2\pi f \frac{d_t + d_r}{c}} g(d_t, d_r) f_(\boldsymbol{\omega_t}, \boldsymbol{\omega_r}). \tag{9}$$

III. Object Reconstruction

The hidden object reconstruction problem is to solve the inverse problem of (6), i.e., finding $\boldsymbol{v}$ given the $\boldsymbol{\tau}$. Since the transform matrix $\boldsymbol{H}$ is poor conditioned and the noise exists in the measurements. Therefore, it is necessary to include the regularization term to improve the reconstruction.

We formulate the inverse problem as an optimization problem. The low-rank nature of the target surface enables us to adopt low-rank optimization to reconstruct the object. Specifically, we first introduce a new variable $\boldsymbol{X}$, which is the 3-D form of $\boldsymbol{v}$, i.e., the 3-D object to be reconstructed. Since we already know the coordinate of antennas and points to be reconstructed, the transform matrix $\boldsymbol{H}$ can be obtained. Thus, the optimization problem can be formulated as

$$\begin{aligned} min \quad & \frac{1}{2} \|\boldsymbol{Hv} - \boldsymbol{\tau}\|_F^2 + \lambda \|\boldsymbol{X}\|_{\omega,*} \\ s.t. \quad & \boldsymbol{v} = reshape(\boldsymbol{X}), \end{aligned} \tag{10}$$

where $\|\boldsymbol{X}\|_{\omega,*}$ is the weighted nuclear norm of matrix X

$$\|\boldsymbol{X}\|_{\omega,*} = \sum_i |\omega_i \sigma_i(\boldsymbol{X})|_1, \tag{11}$$

$\sigma_i(\boldsymbol{X})$ means the i^{th} singular value of $\boldsymbol{X}$, $\boldsymbol{\omega} = [\omega_1, \omega_2, ..., \omega_n]$ and $\omega_i \geq 0$ is a non-negative weight assigned to $\sigma_i(\boldsymbol{X})$.

We bring the constraint into the objective function as the form of augmented Lagrangian:

$$\begin{aligned} \boldsymbol{L}_\rho(\boldsymbol{v}, \boldsymbol{X}, y) =& \frac{1}{2} \|\boldsymbol{Hv} - \boldsymbol{\tau}\|_F^2 \\ &+ \lambda \|\boldsymbol{X}\|_{\omega,*} + y^T(\boldsymbol{v} - reshape(\boldsymbol{X})) \\ &+ \frac{\rho}{2} \|\boldsymbol{v} - reshape(\boldsymbol{X})\|_F^2 \end{aligned} \tag{12}$$

where y is the Lagrange multiplier, and ρ is the penalty factor.

The optimization problem can be solved efficiently by using the alternate direction method of multipliers method (ADMM). For convenience, the scaled form augmented Lagrangian is used for ADMM by adopting scaled dual variable $u = (1/\rho)y$ instead of the Lagrange multiplier y:

$$\begin{aligned} \boldsymbol{L}_\rho(\boldsymbol{v}, \boldsymbol{X}, u) =& \frac{1}{2} \|\boldsymbol{Hv} - \boldsymbol{\tau}\|_F^2 + \lambda \|\boldsymbol{X}\|_{\omega,*} \\ &+ \frac{\rho}{2} \|\boldsymbol{X} - reshape(\boldsymbol{v} + u)\|_F^2 . \end{aligned} \tag{13}$$

ADMM now minimizes $\boldsymbol{L}(\boldsymbol{v}, \boldsymbol{X}, u)$ w.r.t. one variable at a time while fixing the remaining variables. The minimization is then done iteratively by alternately updating $\boldsymbol{v}, \boldsymbol{X}, u$. The key steps of this algorithm are as follows:

$$\begin{aligned} \boldsymbol{v}^{k+1} &= \arg\min_{\boldsymbol{v}} \boldsymbol{L}(\boldsymbol{v}, \boldsymbol{X}^k, u^k) \\ &= \arg\min_{\boldsymbol{v}} \frac{1}{2} \|\boldsymbol{Hv} - \boldsymbol{\tau}\|_F^2 \\ &+ \frac{\rho}{2} \left\|\boldsymbol{X}^k - reshape(\boldsymbol{v} + u^k)\right\|_F^2 \\ &= \frac{\boldsymbol{H}^T\boldsymbol{\tau} + \rho(reshape(\boldsymbol{X}^k) + u^k)}{\boldsymbol{H}^T\boldsymbol{H} + \rho}. \end{aligned} \tag{14}$$

Then we update the 3D object $\boldsymbol{X}$

$$\begin{aligned} \boldsymbol{X}^{k+1} &= \arg\min_{\boldsymbol{X}} \boldsymbol{L}(\boldsymbol{v}^{K+1}, \boldsymbol{X}, u^k) \\ &= \arg\min_{\boldsymbol{X}} \lambda \|\boldsymbol{X}\|_{\omega,*} \\ &+ \frac{\rho}{2} \left\|\boldsymbol{X} - reshape(\boldsymbol{v}^{(\boldsymbol{k+1})} + u^{(k)})\right\|_F^2 \\ &= \boldsymbol{P} S_\omega(\Sigma) \boldsymbol{Q}^T, \end{aligned} \tag{15}$$

where $\boldsymbol{Y}^k = reshape(\boldsymbol{v}^{(k+1)} - u^{(k)}) = \boldsymbol{P}\Sigma\boldsymbol{Q}^T$, and $S_\omega(\Sigma)_{ii} = max(\Sigma_{ii} - \omega_i, 0)$.

The updating of $\boldsymbol{X}$ is similar to that in [13]. As a 3D volume, the SVD of $\boldsymbol{X}$ can only be computed slice by slice. There are many repeated local patterns across a slice because of nonlocal self-similarity, which can be utilized to improve the reconstruction. Thus, we update the slice of $\boldsymbol{X}$ patch by patch. For a local patch y_j in image $\boldsymbol{Y}_i^k$(the i_th slice of $\boldsymbol{Y}^k$), we can search for its nonlocal similar patches across the image by block matching, and stack these similar patches into a

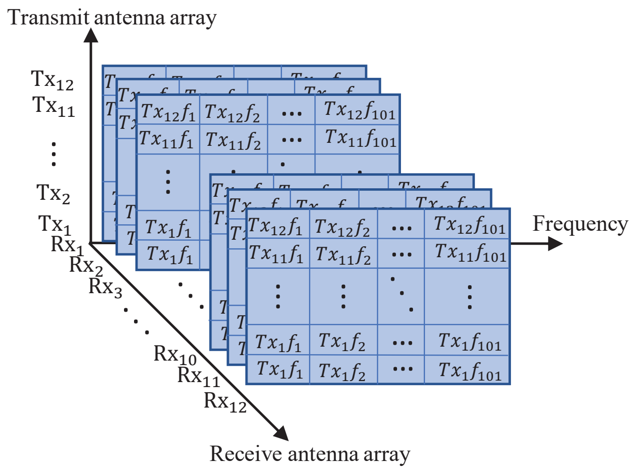

Fig. 6. The measurements are recorded as a 3D complex matrix, where three dimensions represent transmitter antenna, receiver antenna and frequency, respectively.

matrix $\boldsymbol{Y}_{ij}^k$. A patch group of $\boldsymbol{X}^k$ can then be obtained from $\boldsymbol{Y}_{ij}^k$ according to (15). All the patch groups are aggregating together to form $\boldsymbol{X}_i^k$. Finally, all slices $\boldsymbol{X}_i^k$ are aggregating together to form $\boldsymbol{X}^k$.

The final step of the ADMM algorithm is to update the Lagrange dual variable by adding the (scaled) error:

$$u^{k+1} = u^k + \rho(reshape(\boldsymbol{X}^{(k+1)}) - \boldsymbol{v}^{(\boldsymbol{k+1})}). \tag{16}$$

IV. Implementation

A. Simulation setup

In our imaging system, there are two linear arrays placed along the x-axis and the y-axis, respectively. Each array contains 12 antennas spacing 2.6cm apart. The array placed on the x-axis works as the receiver, while the other array works as the transmitter. Thus, we build a 12×12 MIMO system that enables 3D object reconstruction. We assume that the radio signal scatters isotropically from the object.

We utilize the stepped frequency signal as the transmitted signal whose frequency range is 4 GHz to 8 GHz with a 40 MHz frequency step. By sweeping signal among all frequency points, we can obtain frequency-related measurements. According to the image formation model, measurements can be computed by (5). Measurements can be represented as a 3D complex matrix. Three dimensions represent transmitter antenna, receiver antenna and frequency, respectively. The measurements generated from the proposed 12×12 TX and RX channel combination are illustrated in Fig.6.

B. Simulation result

We first simulate two cases with letter “H” and letters “LT”. The letter “H” in the first case is 38cm by 38cm, while the letters “LT” in the second case are 30cm by 30cm. The reconstructed results are shown in Fig.7 and Fig.8. We can see

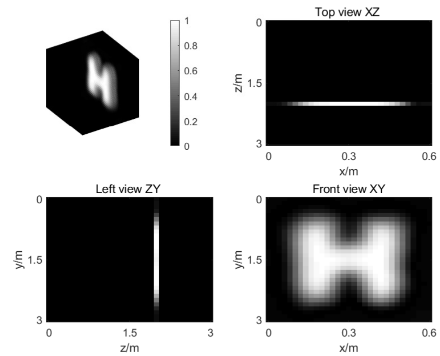

Fig. 7. Reconstruction result of letter “H”.

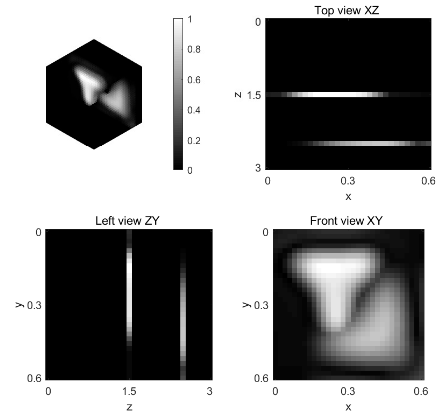

Fig. 8. Reconstruction result of letters “LT”.

that the proposed method can well reconstruct the shape and the depth of the letters.

We then compare the proposed method with recent optical NLOS imaging methods including LCT [1], filtered back projection[10], phasor[14], and Conv [12]. The hidden object is a letter ”T” with width 60cm. To simulate the LCT approach operates in a confocal scanning pattern, the 12×12 MIMO transceiver should be replaced by an equivalent confocal scan grid consists of 12×12 points. As we utilize the steeped-frequency signal with a bandwidth of 4 GHz, the corresponding time resolution is 0.25ns. Then, we can generate light transient according to the image formation model in [1]. The reconstruction results as shown in Fig.9. We can see that with fewer scan points and lower time resolution, the optical NLOS imaging approaches do not perform as well as ours. This is mainly because the optical NLOS imaging methods are sensitive to the time resolution.

Next, we simulate the case with the setup in[1], i.e., the confocal scan grid consists of 32×32 points, the time resolution is 16ps, and the number of time points is 1024. The corresponding reconstruction results as shown in Fig.10. We can see that, even with a much more simple setup,

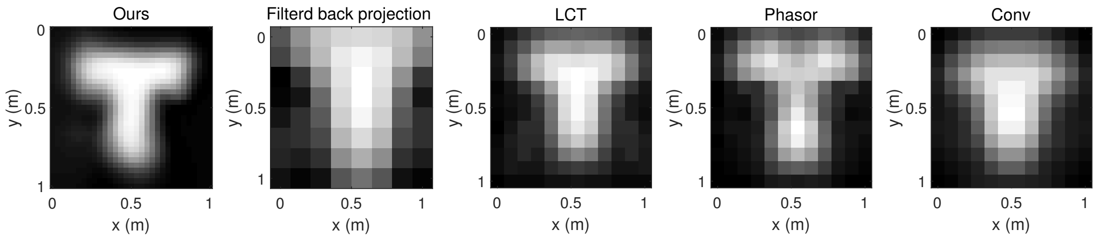

Fig. 9. Comparison between optical NLOS reconstructions and our radio NLOS reconstruction with 0.25ns measurement time resolution.

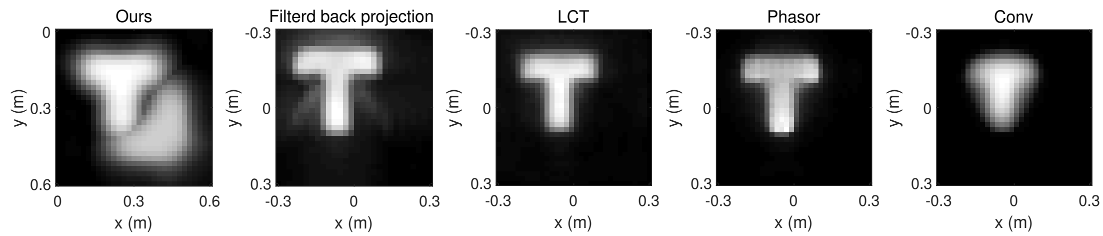

Fig. 10. Comparison between optical NLOS reconstructions and our radio NLOS reconstruction. Our reconstruction recovers the "LT" with 0.25ns measurement time resolution, while optical reconstructions fail to recover the "L" even with 16ps measurement time resolution since the "L" is out the range that can be recovered by the optical signal.

i.e., 12×12 MIMO array and 4GHz bandwidth, the proposed method can achieve comparable reconstruction for the letter "T". Moreover, our method can recover "L" which is $3m$ away from the array while the optical methods fail. This is due to the largest range that could be recovered by optical NLOS imaging is limited by the photon detector, i.e., with 1024 time points the range iccs is equal to $1024 \times 16e^{-12} * c/2 = 2.4576m$.

V. Conclusion

In this paper, we propose to perform NLOS imaging with radio signals. We formulate the imaging problem as a low-rank optimization problem and utilize the ADMM to solve the optimization. With simulations, we show that the proposed method can capture 3D geometry at longer ranges with shorter acquisition times, compared with the optical NLOS imaging methods.

References

[1] M. O'Toole, D. B. Lindell, and G. Wetzstein, "Confocal non-line-of-sight imaging based on the light-cone transform," *Nature*, vol. 555, no. 7696, pp. 338–341, 2018.

[2] K. B. Cooper, R. J. Dengler, N. Llombart, T. Bryllert, G. Chattopadhyay, E. Schlecht, J. Gill, C. Lee, A. Skalare, I. Mehdi *et al.*, "Penetrating 3-d imaging at 4-and 25-m range using a submillimeter-wave radar," *IEEE Transactions on Microwave Theory and Techniques*, vol. 56, no. 12, pp. 2771–2778, 2008.

[3] J. P. Guillet, B. Recur, L. Frederique, B. Bousquet, L. Canioni, I. Manek-Hönninger, P. Desbarats, and P. Mounaix, "Review of terahertz tomography techniques," *Journal of Infrared, Millimeter, and Terahertz Waves*, vol. 35, no. 4, pp. 382–411, 2014.

[4] K. B. Cooper, R. J. Dengler, N. Llombart, B. Thomas, G. Chattopadhyay, and P. H. Siegel, "Thz imaging radar for standoff personnel screening," *IEEE Transactions on Terahertz Science and Technology*, vol. 1, no. 1, pp. 169–182, 2011.

[5] F. Friederich, W. Von Spiegel, M. Bauer, F. Meng, M. D. Thomson, S. Boppel, A. Lisauskas, B. Hils, V. Krozer, A. Keil *et al.*, "Thz active imaging systems with real-time capabilities," *IEEE Transactions on Terahertz Science and Technology*, vol. 1, no. 1, pp. 183–200, 2011.

[6] X. Zhuge and A. G. Yarovoy, "A sparse aperture mimo-sar-based uwb imaging system for concealed weapon detection," *IEEE Transactions on Geoscience and Remote Sensing*, vol. 49, no. 1, pp. 509–518, 2010.

[7] ——, "Three-dimensional near-field mimo array imaging using range migration techniques," *IEEE Transactions on Image Processing*, vol. 21, no. 6, pp. 3026–3033, 2012.

[8] F. Adib, C.-Y. Hsu, H. Mao, D. Katabi, and F. Durand, "Capturing the human figure through a wall," *ACM Transactions on Graphics (TOG)*, vol. 34, no. 6, pp. 1–13, 2015.

[9] A. Kirmani, T. Hutchison, J. Davis, and R. Raskar, "Looking around the corner using ultrafast transient imaging," *International journal of computer vision*, vol. 95, no. 1, pp. 13–28, 2011.

[10] A. Velten, T. Willwacher, O. Gupta, A. Veeraraghavan, M. G. Bawendi, and R. Raskar, "Recovering three-dimensional shape around a corner using ultrafast time-of-flight imaging," *Nature communications*, vol. 3, no. 1, pp. 1–8, 2012.

[11] F. Heide, L. Xiao, W. Heidrich, and M. B. Hullin, "Diffuse mirrors: 3d reconstruction from diffuse indirect illumination using inexpensive time-of-flight sensors," in *Proceedings of the IEEE Conference on Computer Vision and Pattern Recognition*, 2014, pp. 3222–3229.

[12] B. Ahn, A. Dave, A. Veeraraghavan, I. Gkioulekas, and A. C. Sankaranarayanan, "Convolutional approximations to the general non-line-of-sight imaging operator," in *Proceedings of the IEEE International Conference on Computer Vision*, 2019, pp. 7889–7899.

[13] S. Gu, L. Zhang, W. Zuo, and X. Feng, "Weighted nuclear norm minimization with application to image denoising," in *2014 IEEE Conference on Computer Vision and Pattern Recognition*, 2014, pp. 2862–2869.

[14] X. Liu, I. Guillén, M. La Manna, J. H. Nam, S. A. Reza, T. H. Le, A. Jarabo, D. Gutierrez, and A. Velten, "Non-line-of-sight imaging using phasor-field virtual wave optics," *Nature*, vol. 572, no. 7771, pp. 620–623, 2019.